Cerium and zinc: Dual-doped LiMn$_2$O$_4$ spinels as cathode material for use in lithium rechargeable batteries

R. Thirunakaran [a], A. Sivashanmugam [a], S. Gopukumar [a,*], R. Rajalakshmi [b]

[a] Central Electrochemical Research Institute, Karaikudi-630 006, Tamil Nadu, India
[b] A.V.V.M. Sri Pushpam College, Poondi, Thanjavur, Tamil Nadu, India

ARTICLE INFO

ABSTRACT

Pristine spinel lithium manganese oxide (LiMn$_2$O$_4$) and zinc- and cerium-doped lithium manganese oxide [LiZn$_x$Ce$_y$Mn$_{2-x-y}$O$_4$ (x = 0.01–0.10; y = 0.10–0.01)] are synthesized for the first time via the sol–gel route using p-amino benzoic acid as a chelating agent to obtain micron-sized particles and enhanced electrochemical performance. The sol–gel route offers shorter heating time, better homogeneity and control over stoichiometry. The resulting spinel product is characterized through various methods such as thermogravimetic and differential thermal analysis (TG/DTA), Fourier-transform infrared spectroscopy (FT-IR), X-ray diffraction (XRD), scanning electron microscopy (SEM), energy dispersive X-ray analysis (EDAX) and electrochemical galvanostatic cycling studies. Charge–discharge studies of LiMn$_2$O$_4$ samples heated at 850 °C exhibit a discharge capacity of 122 mAh g^{-1} and a corresponding 99% coulombic efficiency in the 1st cycle. The discharge capacity and cycling performance of LiZn$_{0.01}$Ce$_{0.01}$Mn$_{1.98}$O$_4$ is found to be superior (124 mAh g^{-1}), with a low capacity fade (0.1 mAh g^{-1} cycle^{-1}) over the investigated 10 cycles.

1. Introduction

Pristine spinel LiMn$_2$O$_4$ is an attractive candidate for the positive electrode (cathodes) of rechargeable lithium batteries due to its low cost, non-toxic nature and ease of preparation when compared with other layered oxides such as lithium cobalt oxide (LiCoO$_2$) and lithium nickel oxide (LiNiO$_2$) [1–3]. LiCoO$_2$ has many disadvantages such as high cost, a negative environmental impact and a low practical specific capacity against its theoretical value. It has been reported by several authors that the capacity of pure spinel LiMn$_2$O$_4$ diminishes upon extended cycling at elevated temperatures [4,5]. The capacity fading is due to various factors such as Jahn–Teller distortion, a two-phase unstable reaction [2], slow dissolution of manganese into the electrolyte [6], lattice instability [7] and particle-size distribution [8,9]. To suppress the Jahn–Teller distortion and obtain high cycling capacity, many researchers have studied lithium-rich spinels with various divalent, trivalent and tetravalent-doped spinels such as Co, Zn, Cu, Fe, Ni, Cr, Ga, Ti, and Al [10,11]. Ohuzuku et al. [8] and Lee et al. [12] have reported that partial doping of divalent and trivalent cations is more effective in suppressing the capacity fade during cycling. Furthermore, the capacity fade of LiMn$_2$O$_4$ is often observed in the 3 V region and can be completely suppressed

by doping selenium in LiMn$_2$O$_4$ [13]. Several low-temperature preparation methods, e.g., sol–gel method [14,15], chemical precipitation [16], pechini process and hydrothermal method [17], have been used to obtain cathode materials of required physical and electrochemical properties for use in rechargeable lithium-ion batteries.

Trivalent metal cation (Al^{3+}) was partially doped in LiMn$_2$O$_4$ to enhance the electrochemical stability by Yoshio and coworkers [18]. Oh and coworkers [6,19] reported that the spinel dissolution into the electrolyte resulting from electrochemical oxidation and polarization loss increased cell resistance. Dahn and coworkers [20] reported the performance of a nickel-doped spinel compound synthesized at various conditions. Strobel and coworkers [21] reported that LiAl$_x$Mn$_{2-x}$O$_4$ and LiMg$_{0.5}$Mn$_{1.5}$O$_4$ materials seem to suppress the Jahn–Teller distortion in the Li–Mn–O system and further suggested that aluminium doping through solid solutions is easy because it has an ionic radius (Al^{3+} = 0.57 Å) closer to that of Mn^{3+} (0.66 Å). Al^{3+} ions doped in LiNiO$_2$ [22] was found to stabilize the nickel in the 3$^+$ oxidation state and to suppress capacity fading upon cycling. The work reported here is the first attempt to stabilize the LiMn$_2$O$_4$ spinel structure by a 'green chemistry method' using p-amino benzoic acid as a chelating agent with di- and trivalent cation substitution [LiMn$_2$O$_4$ and LiZn$_x$Ce$_y$Mn$_{2-x-y}$O$_4$ (x = 0.01–0.10; y = 0.10–0.01)]. The sol–gel method provides many advantages such as sub-micron-sized particles, regular morphology, low calcination temperature, better homogeneity, nano-particle size, high surface area and

* Corresponding author. Fax: +91 4565 227779.
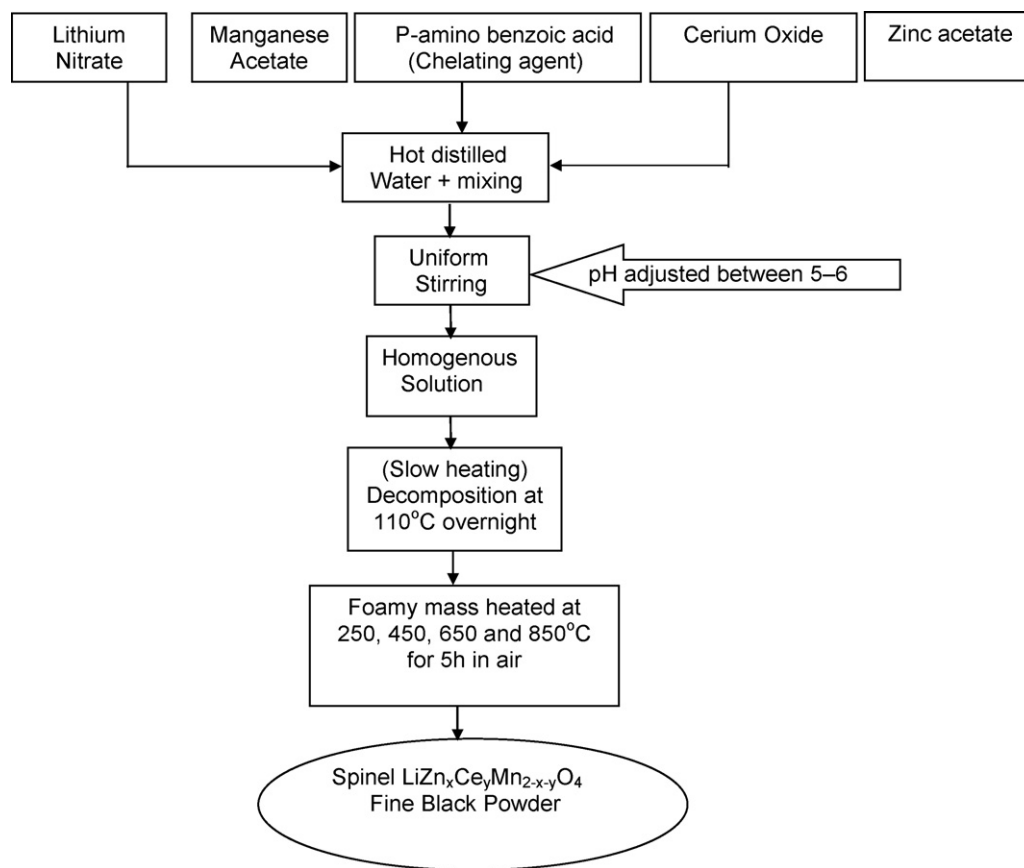E-mail address: deepika_41@rediffmail.com (S. Gopukumar).

Fig. 1. Flow chart for synthesis of $LiZn_xCe_yMn_{2-x-y}O_4$ by sol-gel method using p-amino benzoic acid as chelating agent.

good agglomeration when compared with solid-state synthesis [12].

Ein-Eli et al. [23] reported that divalent metal cations (Zn^{2+}) doped in $LiMn_2O_4$ partially enhanced the electrochemical stability of the compound [23]. Instead of doping Ce^{3+} ions, CeO_2-coated over spinel electrodes was investigated to improve the electrochemical stability of the spinel by Ha et al. [24]. $LiZn_{0.05}Mn_{1.95}O_4$ was examined [25] and found to deliver a capacity of 95 mAh g^{-1} with strong retention over the investigated 65 cycles.

Fig. 2. TG/DTA analysis of spinel $LiMn_2O_4$ precursor.

2. Experimental

Pristine $LiMn_2O_4$ and $LiZn_xCe_yMn_{2-x-y}O_4$: ($x = 0.01, 0.02, 0.05, 0.10$ and $y = 0.10, 0.05, 0.02, 0.01$) powders were synthesized by the sol–gel method using p-amino benzoic acid as a chelating agent. Stoichiometric amounts of lithium nitrate, manganese acetate, zinc acetate, cerium oxide and p-amino benzoic acid were mixed thoroughly and dissolved in de-ionized water. This solution was stirred continuously with gentle heating to achieve homogeneity. Fifty millilitres of 1 M p-amino benzoic acid was added to the highly homogenous solution, and finally a thick gel was obtained. During stirring, the pH was maintained in the range of 5–6. From the obtained gel, small samples were taken for thermogravimetric and differential thermal analysis (TG/DTA) to understand their thermal behaviour in air. The synthesized samples were dried overnight in an oven at 110 °C to remove moisture and thereby obtain the dried mass. The dried mass was ground and calcined at various temperatures, viz., 250, 450, 650 and 850 °C, for 4 h and then characterized via various spectral, microscopic and electrochemical studies. The flowchart in Fig. 1 details the synthesis procedure.

2.1. Electrochemical studies

Coin cells with a 2016 configuration were assembled in an argon-filled glove box (MBraun, Germany) using lithium foil as the anode, Celgard 2400 as the separator, 1 M $LiPF_6$ in a 50:50 (v/v) mixture of ethylene carbonate (EC) and diethylene carbonate (DEC) as the electrolyte, and the synthesized compound as the cathode material. The cathode mix slurry consisted of the synthesized cathode material as active material, conducting carbon and poly-vinylidiene fluoride
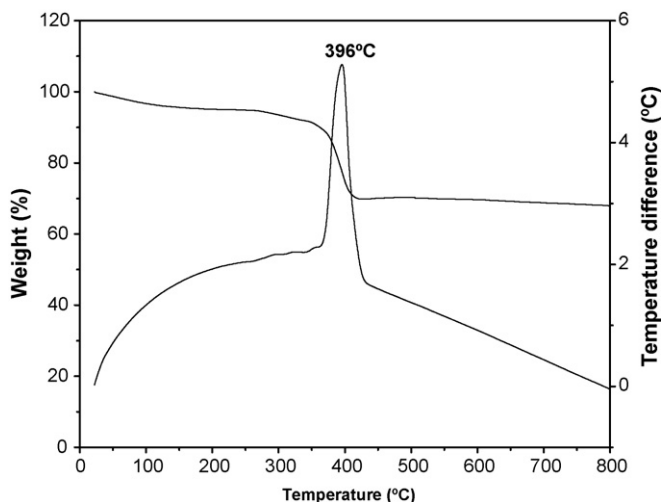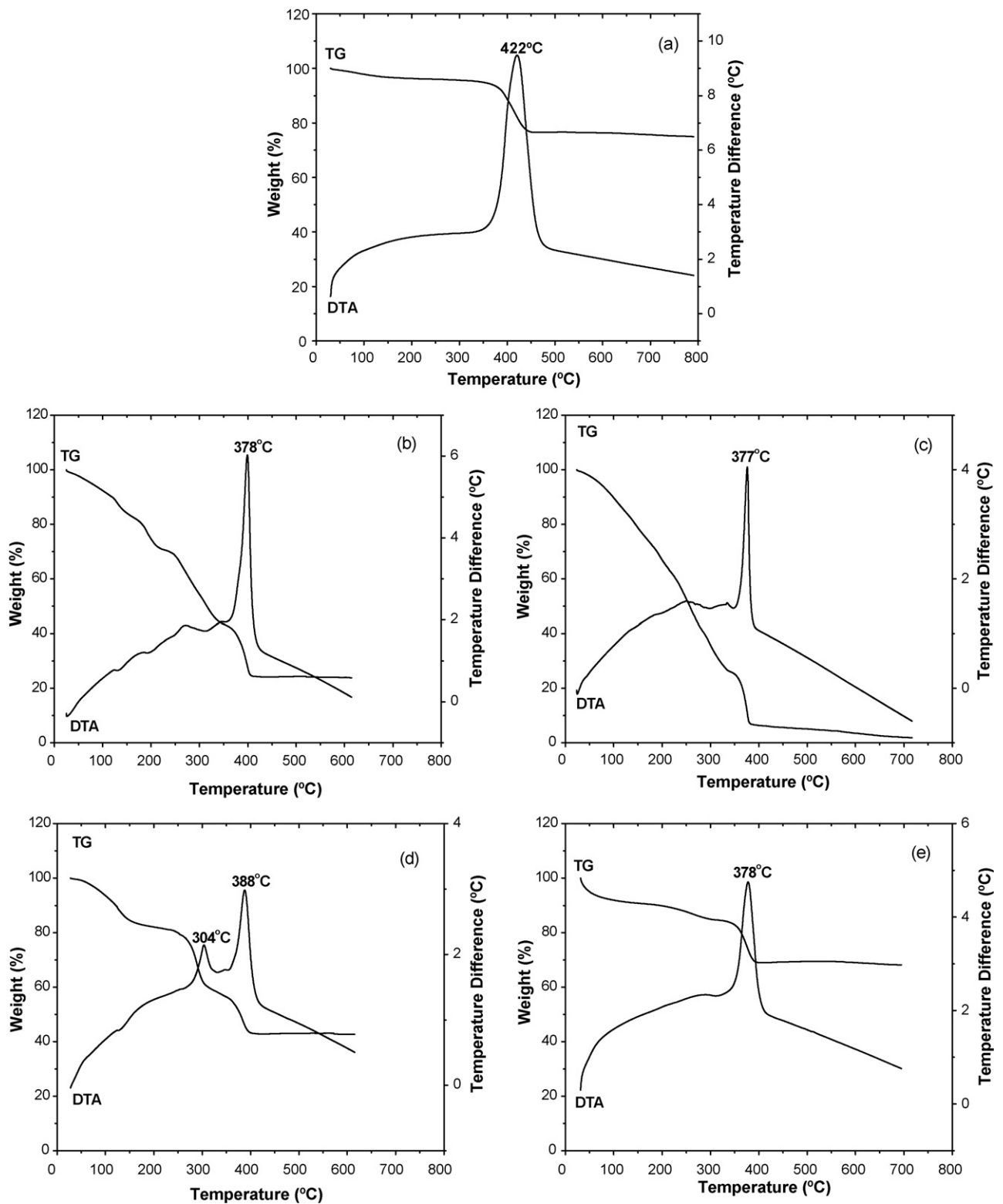
Fig. 3. TG/DTA analysis of $LiZn_xCe_yMn_{2-x-y}O_4$ precursors. (a) Zn: 0.01; Ce: 0.10, (b) Zn: 0.02; Ce: 0.05, (c) Zn: 0.05; Ce: 0.02, (d) Zn: 0.10; Ce: 0.01 and (e) Zn: 0.01; Ce: 0.01.

(PVdF) binder in n-methyl-2-pyrrolidone (NMP) solvent in the ratio 80:10:10. The slurry was coated over aluminium foil and vacuum dried at 110 °C for 2 h. The dried coating was pressed under a 10 t load for 2 min, and electrodes (diameter 18 mm) were punched out and used as the cathode in the coin cell.

The fabricated coin cells were cycled at C/10 rate between 3 and 4.5 V using a battery cycle-life tester.

3. Results and discussion

3.1. Thermal studies

The TGA curve of the spinel $LiMn_2O_4$ precursor is shown in Fig. 2. The TG curve clearly depicts three weight loss zones. Initially, the low weight loss of 5.31% up to 266 °C may be ascribed to the removal
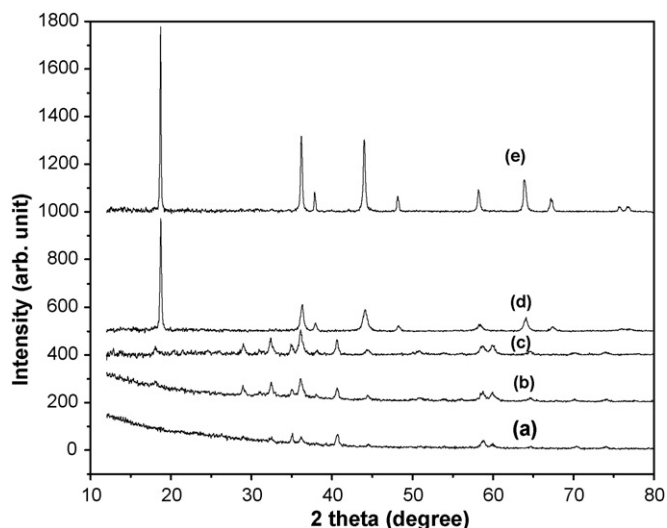
Fig. 4. XRD patterns of $LiMn_2O_4$ samples calcined at different temperatures: (a) as synthesized, (b) 250 °C, (c) 450 °C, (d) 650 °C and (e) 850 °C.

of water. A further region between 344.76 and 415.84 °C corresponds to a major weight loss of 29.61%, which is attributed to the decomposition of the chelating agent (p-amino benzoic acid) and the acetate precursors. The DTA studies show a sharp exothermic peak at 396 °C that indicates the formation of the spinel compound,
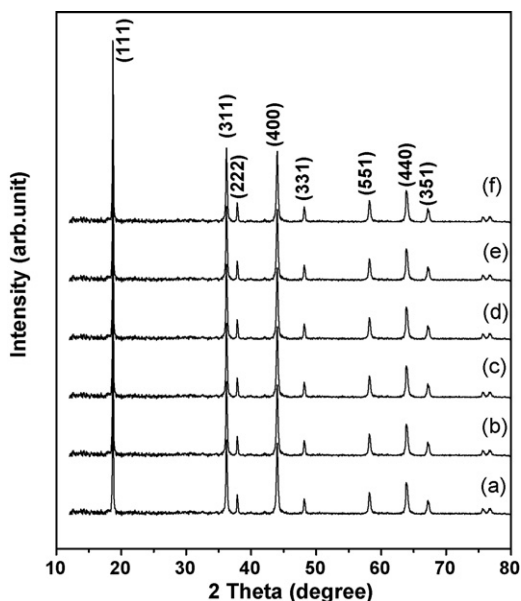

Fig. 5. XRD patterns of spinel $LiMn_2O_4$ and $LiZn_xCe_yMn_{2-x-y}O_4$ particles: (a) undoped, (b) Zn: 0.01; Ce: 0.10, (c) Zn: 0.02; Ce: 0.05, (d) Zn: 0.05; Ce: 0.02, (e) Zn: 0.10; Ce: 0.01, and (f) Zn: 0.01; Ce: 0.01.

Table 1
Unit cell parameters and crystallite size of spinel $LiMn_2O_4$ and $LiZn_xCe_yMn_{2-x-y}O_4$ compounds.

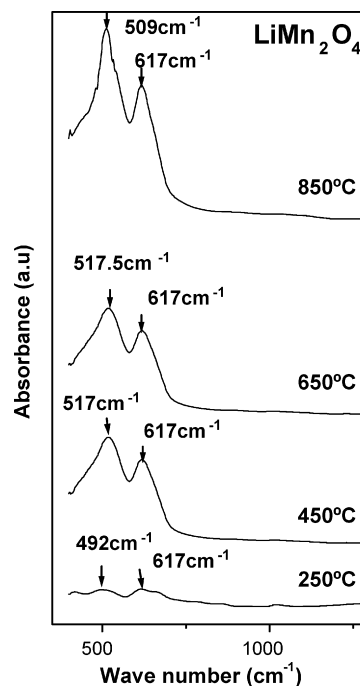| No	Sample	a (Å)	Unit cell volume (Å)^3	Crystallite size × 10^{-9} m
1	$LiMn_2O_4$	8.2339	558	60.17
2	$LiZn_{0.01}Ce_{0.10}Mn_{1.89}O_4$	8.2225	556	60.20
3	$LiZn_{0.02}Ce_{0.05}Mn_{1.93}O_4$	8.2170	555	60.23
4	$LiZn_{0.05}Ce_{0.02}Mn_{1.93}O_4$	8.2395	559	60.25
5	$LiZn_{0.10}Ce_{0.01}Mn_{1.89}O_4$	8.2393	557	60.27
6	$LiZn_{0.01}Ce_{0.01}Mn_{1.98}O_4$	8.2394	559	60.22

Fig. 6. FTIR spectra of $LiMn_2O_4$ particles calcined at different temperatures: 250, 450, 650 and 850 °C.

which correlates with the XRD result given. The peak signatures of $LiMn_2O_4$ are observed when the precursor is calcined at 250 °C. High-intensity peaks, which correspond to a high degree of crystallinity, are observed for samples calcined at 850 °C.

The TG/DTA curves of $LiZn_xCe_yMn_{2-x-y}O_4$ ($x = 0.01$, 0.02, 0.05, 0.10 and 0.01; $y = 0.10$, 0.05, 0.02 and 0.01) precursors synthesized through the sol–gel method using p-amino benzoic acid as the chelating agent are presented in Fig. 3. The thermal behaviour of Zn- and Ce-doped spinels shows characteristic weight
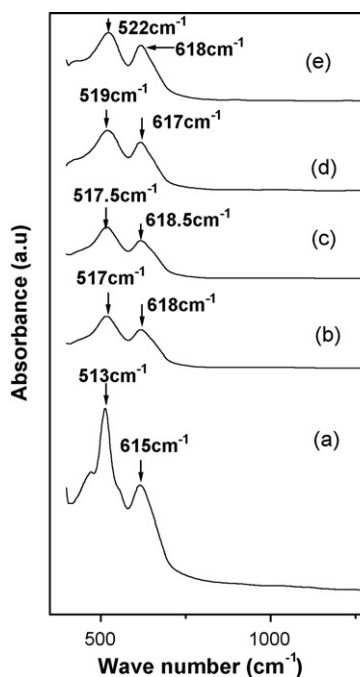

Fig. 7. FTIR spectra of $LiZn_xCe_yMn_{2-x-y}O_4$ particles calcined at 850 °C. (a) $x = 0.01$; $y = 0.10$, (b) $x = 0.02$; $y = 0.05$, (c) $x = 0.05$; $y = 0.02$, (d) $x = 0.10$; $y = 0.01$ and (e) $x = 0.01$; $y = 0.01$.

Table 2
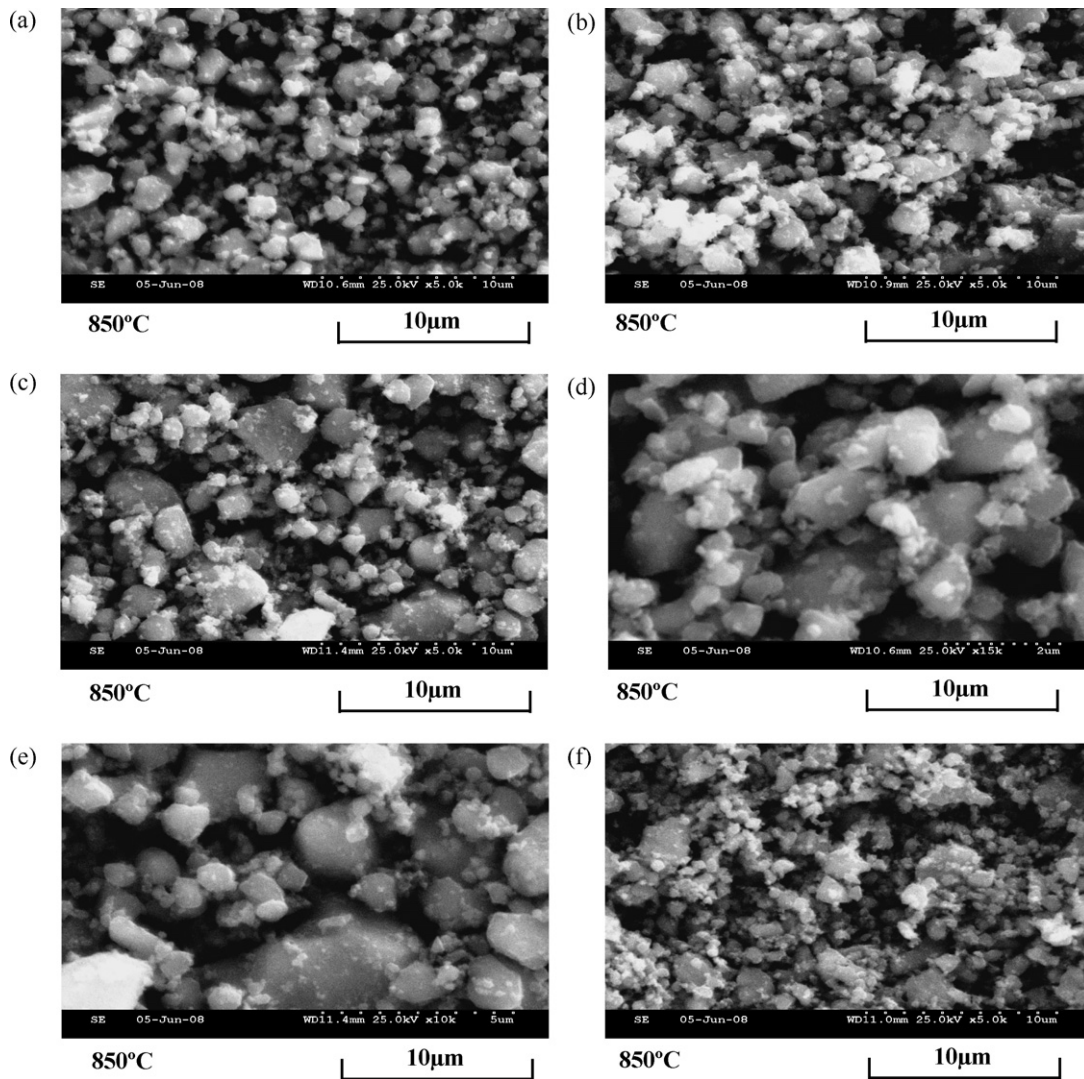FTIR frequencies for peaks observed for $LiMn_2O_4$ calcined at 850 °C.

No	Temperature (°C)	Wave number (cm^{-1})	Assignments
1	250	492	Li–O
		617	Li–Mn–O
2	450	517	Li–O
		617	Li–Mn–O
3	650	518	Li–O
		617	Li–Mn–O
4	850	509	Li–O
		617	Li–Mn–O

Table 3
FTIR frequencies for peaks observed for $LiZn_xCe_yMn_{2-x-y}O_4$ calcined at 850 °C.

No	Sample	Wave number (cm^{-1})	Assignments
1	$LiZn_{0.01}Ce_{0.10}Mn_{1.89}O_4$	513	Li–O
		615	Li–Zn–Ce–Mn–O
2	$LiZn_{0.02}Ce_{0.05}Mn_{1.93}O_4$	517	Li–O
		618	Li–Zn–Ce–Mn–O
3	$LiZn_{0.05}Ce_{0.02}Mn_{1.93}O_4$	518	Li–O
		619	Li–Zn–Ce–Mn–O
4	$LiZn_{0.10}Ce_{0.01}Mn_{1.89}O_4$	519	Li–O
		616	Li–Zn–Ce–Mn–O
5	$LiZn_{0.01}Ce_{0.01}Mn_{1.98}O_4$	522	Li–O
		617	Li–Zn–Ce–Mn–O

loss zones analogous with that of the parent $LiMn_2O_4$. For the $LiZn_{0.01}Ce_{0.10}Mn_{1.89}O_4$ sample, the first weight loss region (5.08%) observed up to 350 °C is due to the removal of moisture. The second weight loss zone of 23.4% occurs up to 453 °C and is attributed to the decomposition of nitrate precursors. The subsequent TG pattern beyond 453 °C does not report any further weight loss. These processes are verified by the appearance of a single exotherm centred at 422 °C in the DTA curve and are indicative of the formation of the spinel product. As seen in Fig. 3b–d, the TG profile varies and has multiple weight loss zones with a weight loss of 60–80%. This char-

acteristic rise in weight loss may be attributed to the increase in concentration of Zn precursors that have a higher specific heat. The concentration of Zn increases from 0.02 to 0.1 units. This tendency corresponds to the emergence of an additional peak at around 300 °C, and becomes more pronounced with increasing Zn concentration (see Fig. 3d). In all cases, the weight loss zones up to 250 °C may be assigned to the removal of moisture, and major formation of the spinel occurs at around 380–390 °C. This 30 °C fall in the for-

Fig. 8. SEM images of $LiMn_2O_4$ and $LiZn_xCe_yMn_{2-x-y}O_4$. (a) $LiMn_2O_4$, (b) Zn: 0.01; Ce: 0.10, (c) Zn: 0.02; Ce: 0.05, (d) Zn: 0.05; Ce: 0.02, (e) Zn: 0.10; Ce: 0.01 and (f) Zn: 0.01; Ce: 0.01.
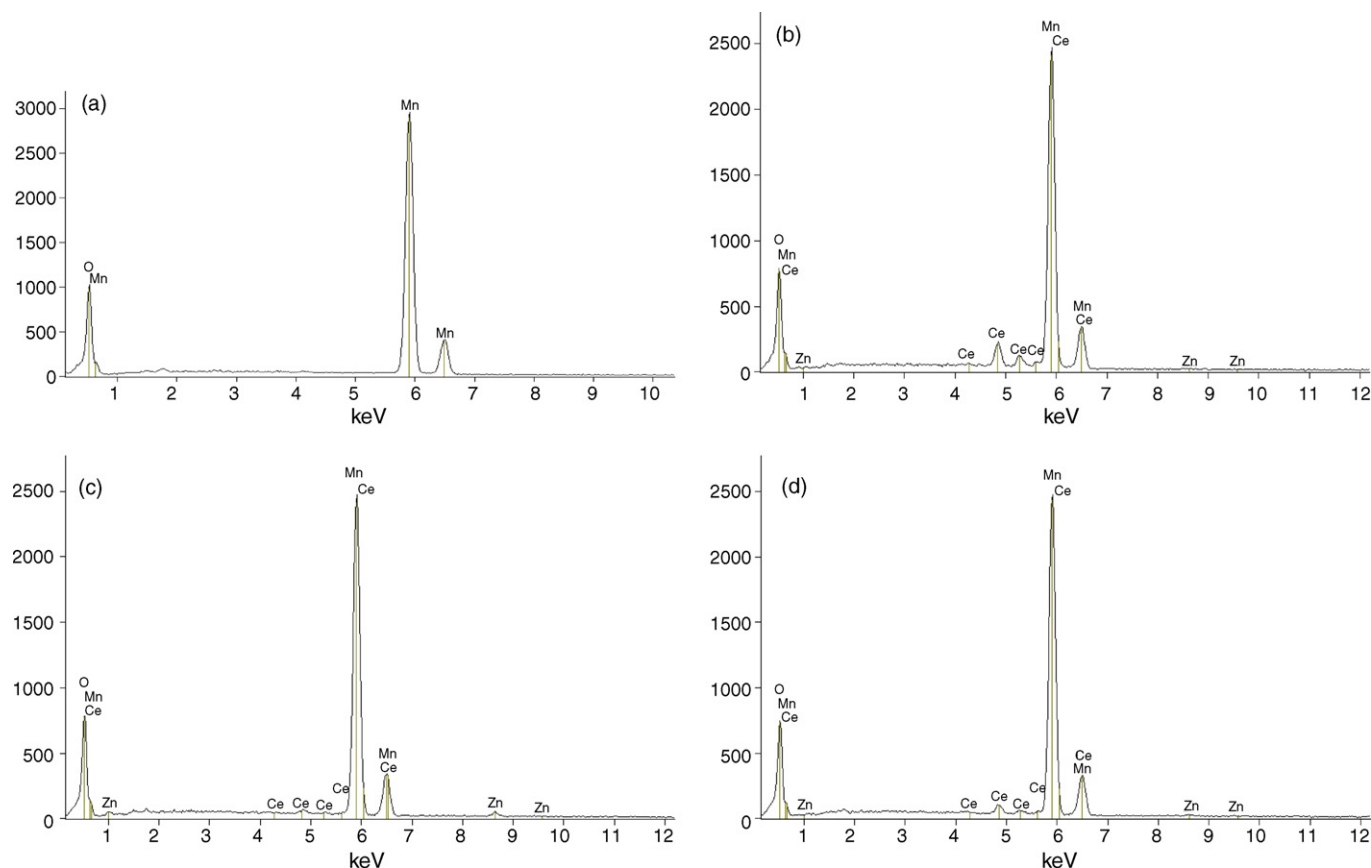
Fig. 9. (a) EDAX profile of LiMn$_2$O$_4$ calcined at 850 °C. (b) EDAX profile of LiZn$_{0.01}$Ce$_{0.10}$Mn$_{1.89}$O$_4$ calcined at 850 °C. (c) EDAX profile of LiZn$_{0.02}$Ce$_{0.05}$Mn$_{1.93}$O$_4$ calcined at 850 °C. (d) EDAX profile of LiZn$_{0.01}$Ce$_{0.01}$Mn$_{1.93}$O$_4$ calcined at 850 °C.

mation temperature observed with the doped precursors leads to the assumption that the precursors form a eutectic mixture, which causes the reaction to proceed much earlier and involves lower heat energy as indicated in the DTA curve. Furthermore, the reaction proceeds as a two-stage process centred at around 304 and 388 °C (Fig. 3d). The TG/DTA profiles in Fig. 3e show similar behaviour to that of Fig. 3a, and the formation of the spinel product occurs at around 378 °C. All precursors have thermally inactive regions after the formation of the spinel product, and thereby imply the closure of thermal events.

3.2. X-ray diffraction studies

Fig. 4 presents the XRD patterns of LiMn$_2$O$_4$ samples calcined at different temperatures: (a) as synthesized; (b) 250 °C; (c) 450 °C; (d) 650 °C; (e) 850 °C. As synthesized and the samples calcined at 250 °C give broad and indistinct reflections that demonstrate the amorphous nature of the compounds. Also, the X-ray reflection of LiMn$_2$O$_4$ calcined at 450 °C and above exhibits a few impurity peaks such as those of α-Mn$_2$O$_3$ and LiMn$_2$O$_3$. The high-intensity spectral profiles such as (1 1 1), (3 1 1), (2 2 2), (4 0 0), (3 3 1), (5 5 1), (4 4 0) and (3 5 1) obtained for samples calcined at 850 °C depict the phase-pure structure and formation of a highly crystalline spinel, which is in good agreement with previous reports [26–28]. The pristine spinel has an Fd3m space group wherein lithium occupies the 8a tetrahedral sites, and manganese ions occupy the 16d sites.

The XRD patterns of LiMn$_2$O$_4$ and LiZn$_x$Ce$_y$Mn$_{2−x−y}$O$_4$ are shown in Fig. 5 with different stoichiometric amounts of divalent and trivalent metal cations, viz., Zn and Ce (Zn–0.01–0.1; Ce–0.1–0.01), synthesized via the sol–gel route calcined at 850 °C. All the peak reflections perfectly match with the Joint Committee on Power Diffraction Standard (JCPDS card No. 35-782). Spectral profiles of undoped and Zn- and Ce-doped spinels exhibit a high degree of crystallinity and better phase purity. It is evident that all the peaks corresponding to (1 1 1), (3 1 1), (2 2 2), (4 0 0), (3 3 1), (5 5 1), (4 4 0) and (3 5 1) hold striking similarity to those reported in a previous communication [29]. Also, some additional peaks are observed at (2 2 2), (3 3 1) and (3 5 1), which may be attributed to the formation of α-Mn$_2$O$_3$ and LiMn$_2$O$_3$. The use of p-amino benzoic acid as a chelating agent facilitates the formation of the metal ligand chain between Mn–O and COO$^−$ that results in the formation of a LiZn$_x$Ce$_y$Mn$_{2−x−y}$O$_4$ spinel product. Table 1 lists the crystallite sizes of the spinel LiMn$_2$O$_4$ and LiZn$_x$Ce$_y$Mn$_{2−x−y}$O$_4$ compounds, and unit cell parameters have been calculated from the XRD data.

3.3. FT-IR spectroscopy studies

The FT-IR spectra of the sol–gel-derived LiMn$_2$O$_4$ powders calcined at different temperatures (250, 450, 650 and 850 °C) are presented in Fig. 6. FT-IR studies on spinel LiMn$_2$O$_4$ have been undertaken by Pimentel et al. [30]. Details of the wave number corresponding to the LiMn$_2$O$_4$ and LiZn$_x$Ce$_y$Mn$_{2−x−y}$O$_4$ spinels are given in Tables 2 and 3. The IR spectral bands are indistinct for the sample calcined at 250 °C and are observed at wavelengths around 492 cm^{-1}, which may be attributed to the Li–O bending vibration mode. The peak around 617 cm^{-1} is assignable to the Li–Mn–O stretching vibration band. It is evident that the spectral reflections at different calcination temperatures reflect a similar behaviour to the Li–Mn–O stretching vibration band. Furthermore, the IR bands for samples calcined at high temperature are shifted slightly towards a higher wave number (509 cm^{-1}).
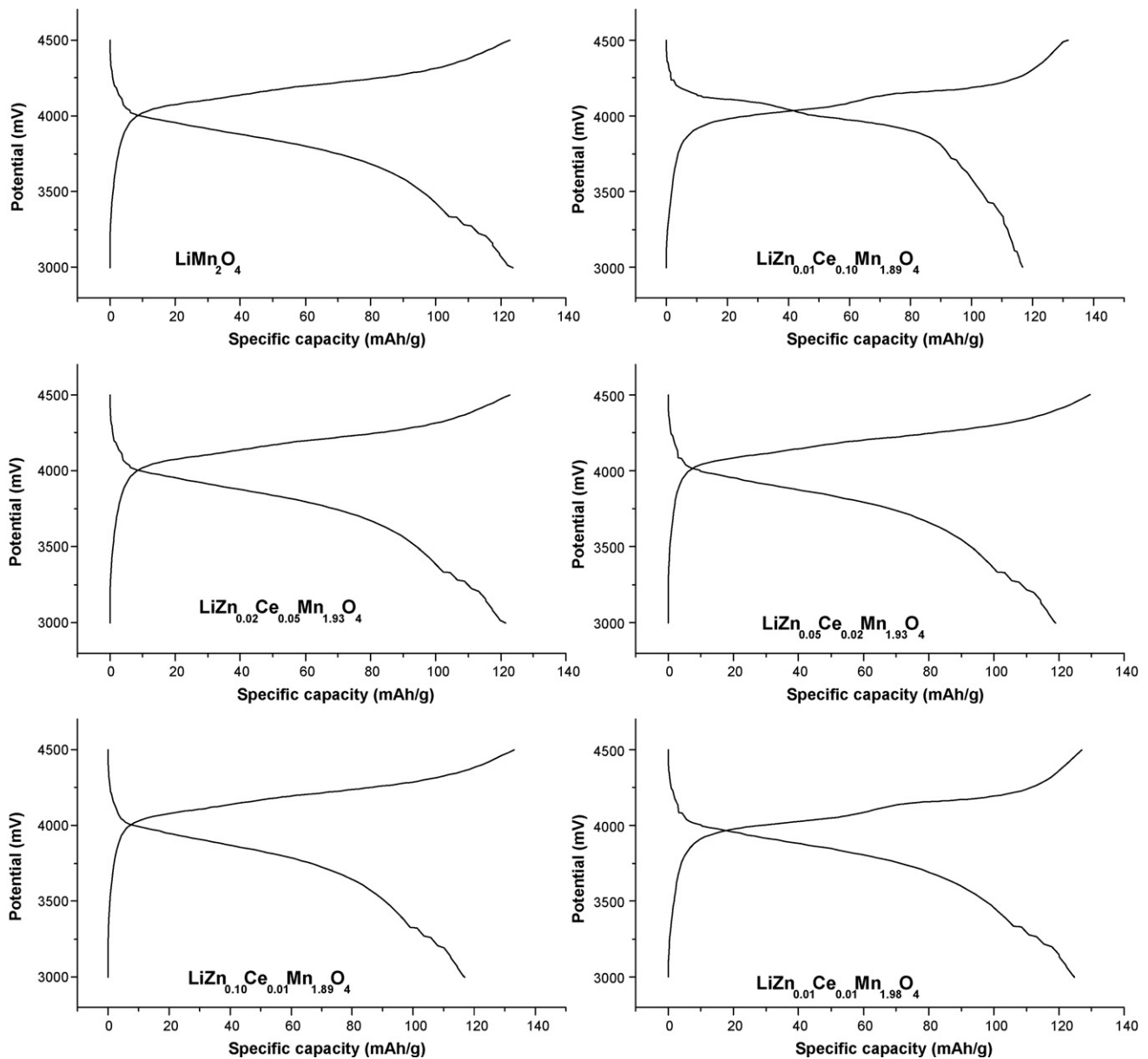
Fig. 10. Charge–discharge behaviour of $LiMn_2O_4$ and $LiZn_xCe_yMn_{2-x-y}O_4$ particles calcined at 850 °C.

Fig. 7 gives FT-IR spectra of undoped and doped $LiMn_2O_4$ with varying amounts of Zn and Ce calcined at 850 °C: (a) Zn–0.01; Ce–0.10, (b) Zn–0.02; Ce–0.05, (c) Zn–0.05; Ce–0.02, (d) Zn–0.10; Ce–0.01, (e) Zn–0.01; Ce–0.01. For Zn- and Ce-doped spinels, the IR spectral bands at lower wave numbers between 513 and 522 cm^{-1} may be ascribed to the Li–O bending vibration, and the peaks observed at higher wave numbers between 615 and 617 cm^{-1} correspond to the Li–Zn–Ce–Mn–O stretching vibration band.

3.4. SEM and EDAX analyses

Fig. 8 shows SEM images of undoped and $LiZn_xCe_yMn_{2-x-y}O_4$ spinel powders: (a) pure spinel $LiMn_2O_4$, (b) Zn = 0.01; Ce = 0.10, (c) Zn = 0.02; Ce = 0.05, (d) Zn = 0.05; Ce = 0.02, (e) Zn = 0.10; Ce = 0.01, (f) Zn = 0.01; Ce = 0.01. The SEM image for the parent $LiMn_2O_4$ calcined at 850 °C (Fig. 8a) reveals an average grain size of 1 μm. The particles of doped-samples are spherical grains and grow in size as the dopant level increases. For the $LiZn_{0.01}Ce_{0.01}Mn_{1.98}O_4$ compound calcined at 850 °C, the particles are smaller spherical grains

with an average particle size of 0.5 μm. Thus, it is evident that low doping of Zn and Ce in the spinel may be beneficial for enhancing the electrochemical activity.

Fig. 9(a–d) represent the EDAX profiles of Zn, Ce and Mn in $LiMn_2O_4$ and $LiZn_xCe_yMn_{2-x-y}O_4$ compounds. The profiles of the reflections corresponding to the constituent elements suggest that the compounds are pure.

3.5. Galvanostatic charge–discharge studies

Fig. 10 shows the charge–discharge cycle behaviour of $LiMn_2O_4$ and $LiZn_xCe_yMn_{2-x-y}O_4$ particles with different Zn and Ce stoichiometry viz., (a) $x = 0.00$; $y = 0.00$, (b) $x = 0.01$; $y = 0.10$, (c) $x = 0.02$; $y = 0.05$, (d) $x = 0.05$; $y = 0.02$, (e) $x = 0.10$; $y = 0.01$, (f) $x = 0.01$; $y = 0.01$ calcined at 850 °C. All charge–discharge curves show two plateau regions that indicate de-intercalation/intercalation of lithium ions at the 8a tetrahedral sites. The undoped spinel $LiMn_2O_4$ heated at 850 °C delivers a discharge capacity of 122 mAh g^{-1} against a charging capacity of 123 mAh g^{-1}, which corresponds to 99% coulombic
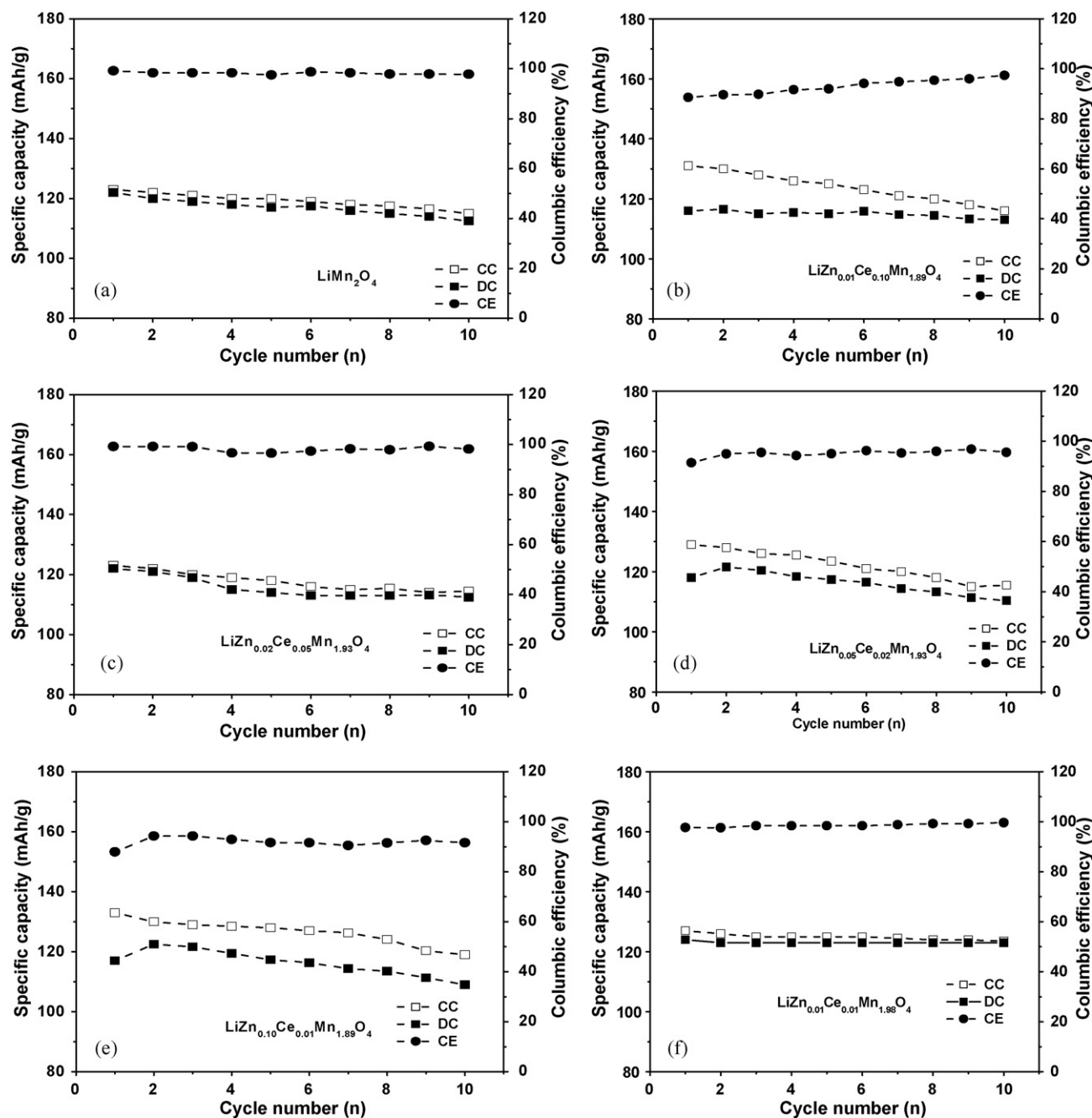
Fig. 11. Cycling behaviour of $LiMn_2O_4$ and $LiZn_xCe_yMn_{2-x-y}O_4$ particles calcined at 850 °C: (a) $x = 0.00$; $y = 0.00$, (b) $x = 0.01$; $y = 0.10$, (c) $x = 0.02$; $y = 0.05$, (d) $x = 0.05$; $y = 0.02$, (e) $x = 0.10$; $y = 0.01$, (f) $x = 0.01$; $y = 0.01$. CC – charge capacity; DC – discharge capacity; CE – Coulombic efficiency.

efficiency in the first cycle. In the 10th cycle, the cell delivers a discharge capacity of 112 mAh g^{-1} or a coulombic efficiency of 98%. The $LiMn_2O_4$ experiences a capacity fade of 0.95 mAh g^{-1} cycle^{-1} over the investigated 10 cycles.

Cells with zinc- and cerium-doped spinels deliver discharge capacities of 116, 122, 118 and 117 mAh g^{-1} on the 1st cycle and experience a capacity fade of 0.3, 1.0, 0.8 and 0.8 mAh g^{-1} cycle^{-1} for the Zn:Ce contents corresponding to 0.01:0.10, 0.02:0.10, 0.05:0.02 and 0.10:0.01, respectively. Several researchers have already reported [31,32] the use of metal cations with high ionic radii as dopants, such as cerium (Ce) and neodymium (Nd) for lithium-ion batteries. It is interesting to note that samples with equal stoichiometric amounts of zinc and cerium ($LiZn_{0.01}Ce_{0.01}Mn_{1.98}O_4$) exhibit superior performance (124 mAh g^{-1}) against a charging capacity of 127 mAh g^{-1} during the first cycle when compared with the parent

$LiMn_2O_4$ and other dopant concentrations. This increase in capacity may be due to a lower cation mixing/distribution of bi- and trivalent dopants so as to stabilize the spinel structure.

The cycling behaviour of undoped and doped spinels calcined at 850 °C over the investigated 10 cycles together with the corresponding coulombic efficiencies (CE) is illustrated in Fig. 11(a–f). During the first cycle, the parent $LiMn_2O_4$ delivers a discharge capacity of 122 mAh g^{-1} against the theoretical capacity of 148.6 mAh g^{-1}. Cycling studies of doped materials suggest that the $LiZn_{0.01}Ce_{0.01}Mn_{1.98}O_4$ compound calcined at 850 °C shows superior performance. Zn-doped spinels [$LiZn_{0.05}Mn_{1.95}O_4$] have been studied [25] and deliver 95 mAh g^{-1} with excellent capacity retention over the investigated 65 cycles. For $LiZn_{0.01}Ce_{0.01}Mn_{1.98}O_4$, the cells exhibit a stable discharge capacity of 124 mAh g^{-1} over the investigated 10 cycles and a low capacity fading of
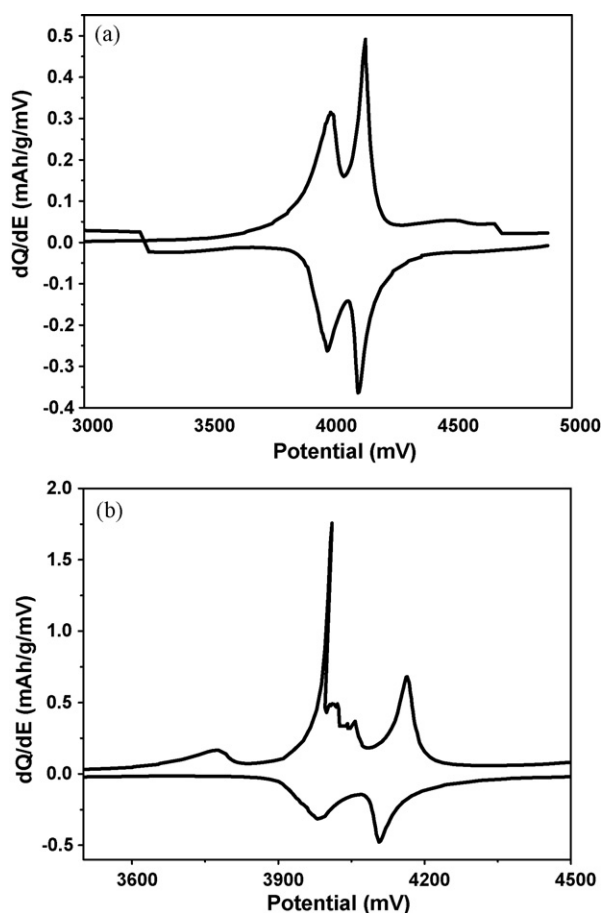
Fig. 12. (a) Differential capacity curve for $LiMn_2O_4$. (b) Differential capacity curve for $LiZn_{0.01}Ce_{0.01}Mn_{1.98}O_4$.

0.1 mAh g^{-1} cycle^{-1} corresponding to a coulombic efficiency of 99%. Higher capacity fade is observed with higher doping up to five cycles. However, after five cycles the capacity stabilized at around 115 mAh g^{-1}, which is lower than the capacity obtained for the $LiZn_{0.01}Ce_{0.01}Mn_{1.98}O_4$ compound. Hence, low levels of zinc and cerium doping exhibit better cycle behaviour and good capacity retention.

3.6. dQ/dE vs. potential curves

The differential capacity curve of the parent $LiMn_2O_4$ calcined at 850 °C is depicted in Fig. 12a. This curve possesses two oxidative peaks during lithium-ion extraction and two reductive peaks for lithium insertion. The first two predominant anodic peaks at about 4.01 and 4.15 V correspond to Mn^{3+}/Mn^{4+} couples with an average oxidation state of 3.5$^+$, whereas the cathodic peaks appearing between 4.12 and 3.99 V are due to reductive behaviour of the spinel. These results are in agreement with earlier reports [29]. Furthermore, it has been shown [11] that the stability of the spinel could be improved by partial doping of metal cations such as Co^{2+}, Al^{3+}, Cu^{2+}, Mg^{2+}, Cr^{3+}, Ti^{4+} and Zn^{2+} [10,11]. In the case of the parent $LiMn_2O_4$, the anodic and cathodic peaks are well defined and suggest that the reactions are first order.

The differential capacity curve of $LiZn_{0.01}Ce_{0.01}Mn_{1.98}O_4$ calcined at 850 °C is clearly shown in Fig. 12b. It is evident that three well-defined anodic peaks, centred at about 3.98 and 4.16 V correspond to the de-intercalation process at the 8a tetrahedral sites associated with Mn^{3+}/Mn^{4+} and Zn^+/Zn^{2+}. The Ce^{2+}/Ce^{3+} couples and cathodic peaks between 4.10 and 3.98 V have been attributed

to the intercalation reaction [24]. The cyclic voltammogram of the CeO_2-coated spinel is strikingly similar to that of our study. The differential capacity curve for the $LiZn_{0.01}Ce_{0.01}Mn_{1.98}O_4$ compound reveals that there is an increase in both the anodic and the cathodic peaks when compared with the undoped spinel. These observations suggest that the low amounts of zinc and cerium in the spinel ($LiZn_{0.01}Ce_{0.01}Mn_{1.98}O_4$) enhance the electrochemical activity.

4. Conclusions

Pristine spinels of $LiMn_2O_4$ and $LiZn_xCe_yMn_{2-x-y}O_4$ ($x = 0.01$–0.10; $y = 0.10$–0.01) have been synthesized for the first time via the sol–gel route using p-amino benzoic acid as the chelating agent to obtain micron-sized particles with enhanced electrochemical performance to use as a cathode material in lithium rechargeable batteries. Scanning electron micrographs images of the parent $LiMn_2O_4$ calcined at 850 °C clearly show that the grains are of micron size. The particles of $LiZn_{0.01}Ce_{0.01}Mn_{1.98}O_4$ calcined at 850 °C appear as smaller spherical grains of 0.5 μm size and are comparatively smaller than for other dopant concentrations. Charge–discharge studies of pristine spinel $LiMn_2O_4$ heated at 850 °C give a discharge capacity of 122 mAh g^{-1} corresponding to 99% coulombic efficiency in the 1st cycle. At the end of the 10th cycle, the cell delivers a discharge capacity of 112 mAh g^{-1} with 99% coulombic efficiency and a capacity fade of 0.95 mAh g^{-1} cycle^{-1}. Among all dopant concentrations investigated, the $LiZn_{0.01}Ce_{0.01}Mn_{1.98}O_4$ sample exhibits the best performance (1st cycle discharge capacity: 124 mAh g^{-1}), with an average discharge capacity of 125 mAh g^{-1} over the 10 cycles and the least capacity fade (0.1 mAh g^{-1} cycle^{-1}).

References

[1] J.M. Tarascon, W.R. McKinnon, F. Coowar, T.N. Bowner, G. Amatucci, D. Guyomard, J. Electrochem. Soc. 141 (1994) 1431.
[2] R.J. Gummow, A. de Kock, M.M. Thackeray, Solid State Ionics 69 (1994) 67.
[3] M.M. Thackeray, A. de Kock, M.H. Rossouw, D. Liles, R. Bittihn, D. Hoge, J. Electrochem. Soc. 139 (1992) 366.
[4] Y. Xia, M. Yoshio, J. Electrochem. Soc. 144 (1977) 2600.
[5] G. Pistoia, A. Antonini, R. Rosati, D. Zane, Electrochim. Acta 41 (1996) 2689.
[6] D.H. Jang, J.Y. Shin, S.M. Oh, J. Electrochem. Soc. 143 (1996) 2211.
[7] A. Yamada, J. Solid State Chem. 122 (1996) 165.
[8] T. Ohuzuku, S. Takeda, M. Iwanaga, J. Power Sources 90 (1999) 82.
[9] D. Song, H. Ikuta, T. Uchida, M. Wakihara, Solid State Ionics 117 (1999) 156.
[10] M. Javed Iqbal, S. Zahoor, J. Power Sources 165 (2007) 397.
[11] G. Kumar, H. Schlorb, D. Rahner, Mat. Chem. Phys. 70 (2001) 123.
[12] J.H. Lee, J.K. Hong, D.H. Jang, Y.K. Sun, S.M. Oh, J. Power Sources 89 (2000) 7–14.
[13] S.H. Park, K.S. Park, Y.K. Sun, K.S. Nahm, J. Electrochem. Soc. 147 (2000) 2121.
[14] S. Bach, M. Henry, N. Baffier, J. Livage, J. Solid State Chem. 88 (1990) 333.
[15] J.P. Perreira-Ramos, J. Power Sources 54 (1995) 126.
[16] P. Barboux, J.M. Tarascon, F.K. Shokoohi, J. Solid State Chem. 94 (1991) 196.
[17] W. Liu, G.C. Farrington, F. Chaput, B.J. Dunn, J. Electrochem. Soc. 143 (1996) 884.
[18] Y.S. Lee, N. Kumada, M. Yoshio, J. Power Sources 96 (2001) 384.
[19] D.H. Jang, Y.J. Shin, S.M. Oh, J. Electrochem. Soc. 144 (1997) 3348.
[20] Q. Zhone, A. Bonakdarpour, M. Zhang, Y. Gao, J.R. Dahn, J. Electrochem. Soc. 144 (1997) 213.
[21] F. Le Cras, D. Bloch, M. Anne, P. Strobel, Solid State Ionics 89 (1996) 203–213.
[22] P. Kalyani, N. Kalaiselvi, N. Muniyandi, J. Electrochem. Soc. 150 (2003) 764.
[23] Y. Ein-Eli, W. Wen, S. Mukherjee, Electrochem. Solid-State Lett. 8 (2005) A144.
[24] H.-W. Ha, N.J. Yun, K. Kim, Electrochim. Acta 52 (2007) 3241.
[25] C. Bellitto, E.M. Bauer, G. Righini, M.A. Green, W.R. Branford, A. Antonini, M. Pasquali, J. Phys. Chem. Solids 65 (2004) 27.
[26] R. Thirunakaran, A. Sivashanmugam, S. Gopukumar, C.W. Dunnill, D.H. Gregory, Mater. Res. Bull. 43 (2008) 2129.

[27] R. Thirunakaran, K.T. Kim, Y.M. Kang, C.Y. Seo, J.Y. Lee, Mater. Res. Bull. 40 (2005) 177.

[28] R. Thirunakaran, A. Sivashanmugam, S. Gopukumar, C.W. Dunnill, D.H. Gregory, J. Phys. Chem. Solids 69 (2008) 2082.

[29] R. Thirunakaran, K.T. Kim, Y.M. Kang, C.Y. Seo, J.Y. Lee, J. Power Sources 137 (2004) 100.

[30] P.M. Pimentel, A.E. Martinelli, D. Maria de Araujo Melo, A.M. Garrido Pedrosa, J.D. Cunha, C.N. Silva Jr, Mater. Res. 8 (2) (2005) 9, doi:10.1590/S1516-14392005000200024.

[31] R. Singhal, S.R. Das, M.S. Tomar, O. Ovideo, S. Nieto, R.E. Melgarejo, R.S. Katiyar, J. Power Sources 164 (2007) 857–861.

[32] Z.S. Peng, Y. Jiang, Z.Y. Jin, J. Rare Earth 17 (2000) 115–119.